Source Properties of a Hollow Cathode Arc Plasma

J. M. M. J. Vogels, L. U. E. Konings *, and D. C. Schram
Eindhoven University of Technology, Eindhoven, The Netherlands

Z. Naturforsch. **41 a**, 585–600 (1986); received November 19, 1985

Experiments have been carried out on the properties of a hollow cathode as an ion-source.
The measured electron density, ion and neutral temperatures and drift velocities have been compared with predictions from the conservation laws for matter, momentum and energy.
Very large exit drift velocities of ions and neutrals are observed. The magnitude and direction, against the electric field, can be explained on the basis of the momentum balance. At weak magnetic field strengths even supersonic drift velocities are found. The charge flux carried by the ions is about five percent of the net arc current. For small flows, the ionized fraction of the gas supply approaches 100%.
The neutral particle density outside the cathode consist of a fraction drifting with a large velocity out of the cathode and a fraction of cool background atoms. The change of the ratio of these fractions with increasing distance to the cathode causes the average neutral particle drift to decrease very rapidly.
Finally, an analysis of the overall cathode power balance is given.

1. Introduction

The magnetized hollow cathode arc is an easily accessible and versatile device for the study of highly ionized plasmas at low density [1–3]. Of the incoming gas flux through the cathode a fraction is ionized which contributes to the formation of an external plasma column. A description of the cathode plasma is important for understanding gas efficiency, power consumption and external arc conditions [4–6]. The complicated nature of the cathode processes however permits detailed descriptions only under rather strict assumptions [7].

Hollow cathodes can be applied in several geometries [8] and modes of operation [9, 10]. We will confine ourselves to the study of the plasma eminating from a cylindrical tantalum tube. As has been pointed out by Delcroix [8] such a cathode has several working regimes: the regime of low gas flow in which the cathode tip has the highest temperature, the low current regime with the presence of cathode spots [11] and the normal mode with a diffuse arc [12, 13] and with the highest temperature at a distance of about the tube diameter from the tip. Most of our experiments have been carried out in the normal mode; at low currents a hot spot indeed has been observed.

A number of important physical phenomena has been studied by several authors. In the heating of the cathode the electrical (Debye) boundary layer plays a major role [14, 15]. This sheath also causes an enhanced thermionic emission of free electrons. The arc crosses the magnetic field inside the cathode, which sets up a rotational force density there. It has been pointed out that metastable particles play a role in the cathode operation [16, 17]; also the volume ionization of neutral particles by electrons that enter the internal plasma with about the sheath potential, is a process of primary importance.

An analysis of the radial current density profile has been carried out in the case of a negligibly small gas flow [17]. Also the ion dynamics may influence the radial currents. It will be shown that the longitudinal ion and neutral drift velocities approach the thermal speed [18] and may even be supersonic just behind the tube exit.

Because the main use of hollow cathodes is in their source properties [19–21] we will consider the mass, momentum and energy conversions of the flowing gas in the cathode as a whole, rather than develop a detailed picture of the physics inside. Nevertheless our experimental data will allow us to make estimates of some internal quantities.

---

* Presently at Nederlandse Philips Bedrijven b.v., Lighting Div., Eindhoven, The Netherlands.

Reprint requests to Prof. Dr. D. C. Schram, Dept. of Physics, Eindhoven University of Technology, P.O. Box 513, 5600 MB Eindhoven, Niederlande.

0340-4811 / 86 / 0400-0585 $ 01.30/0. – Please order a reprint rather than making your own copy.

One of the crucial parameters of the cathode is the longitudinal drift velocity with which the ions and neutrals leave the cathode. With the velocity sampling of an anode extracted beam, Theuws established supersonic velocities [21–23]. This method has the disadvantage that the sampling is performed outside the plasma. So the velocity distribution is measured folded with a transmission probability, which is smaller for low velocity particles. These measurements indicate large velocities of neutrals and metastables but it cannot be excluded that these may originate from a high velocity tail. We will measure the velocity in situ, just behind the cathode exit by the method of Doppler interferometry [24]. These measurements, together with experiments on temperatures and densities, will permit us to draw conclusions on ion production rates, cathode saturation phenomena, momentum balances and the main energy conversion processes in the cathode. By this our program is established.

Our experiments have been carried out on the large scale device at the Eindhoven University of Technology, which has been described elsewhere [4, 12, 13, 25]. As a test gas we use argon.

2. Theory

As a theoretical framework for a diffuse cathode plasma [12] we will consider the conservation laws of matter, longitudinal momentum and energy in the cathode. As stated before, our measurements have been done outside the tube itself. Therefore, an integral formulation of the conservation laws is appropriate. Most of our experiments have been carried out at a longitudinal distance $z = 10$ mm from the cathode tip, so we define this position as the outer boundary in the theory.

2.1. Matter conservation

The gas flow rate N_g, the number of gas particles per second that enters the cathode, must leave it either as neutral gas flow rate ($\dot{N}_a$) or as ion flow rate ($\dot{N}_i$), singly or multiply ionized:

$$\dot{N}_g = \dot{N}_i + \dot{N}_a = (n_i^* A_i^* + n_a^* A_a^*)\, w_z^* . \tag{1}$$

Here n_i^* and n_a^* are the exit particle densities on the axis, w_z^* is the heavy particle longitudinal drift velocity on the axis and A_i^* and A_a^* are the effective cross sections of the ion and neutral flow rates:

$$A^* = \left(\int_0^\infty n\, w_z\, 2\pi r\, \mathrm{d}r \right) / (n\, w_z)_{r=0} . \tag{2}$$

The asterix * refers to a location of observation which is 1 cm downstream from the cathode, $z^* = 10^{-2}$ m.

It is appropriate to relate $\dot{N}_i$ to the charge carrier flux I_a/e, the arc current over the elementary charge. The arc current emerges from free electron emission and from ion recombination at the inner cathode surface. Each spontaneously emitted electron gains about 30 eV energy in the Debye sheath [15] and contributes to direct or stepwise ionization, which indicates a proportionally between $\dot{N}_i$ and I_a/e. The part of I_a which is sustained by ion wall recombination contains a proportionality with n_i^i, the ion density inside the cathode, and is therefore related to $\dot{N}_i$. Nevertheless at very low gas flow, $\dot{N}_i$ is limited by $\dot{N}_g$. So we expect nearly full ionization at sufficiently small $\dot{N}_g$ and a saturation, $\dot{N}_i^{sat}$ of $\dot{N}_i$ if $\dot{N}_g$ is large, with some proportionality between $\dot{N}_i^{sat}$ and I_a/e. The ionized fraction $\alpha = \dot{N}_i/\dot{N}_g$ must decrease from about 1 to 0 as $\dot{N}_g$ varies from 0 upwards.

2.2. Momentum conservation

Concerning the conservation of longitudinal momentum within the cathode tube we distinguish as the main parameters the driving pressure P_g at the entrance of the tube, the kinetic pressure $(n_i^* + n_e^* + n_a^*)\, k_B T^*$ and the convective momentum flux $(n_i^* + n_a^*)\, m\, w_z^{*2}$ at the exit, and the viscous pressure decay ΔP_v along the tube. Here T is the exit temperature, which, because of the high density, is about equal for the different kinds of particles, electrons, ions and neutrals, k_B is the Boltzmann constant and m is the ion mass. We note that the electric field plays no role [24]. We may neglect the momentum contribution of the radial current crossing the azimuthal component of the magnetic field inside the tube. The balance equation reads

$$P_g A^i = ((n_i^* + n_e^*)\, A_i^* + n_a^* A_a^*)\, k_B T^* + (n_i^* A_i^* + n_a^* A_a^*)\, m\, w_z^* + A^i \Delta P_v . \tag{3}$$

Here $A^i = \pi R_1^2$ and R_1 is the inner tube cross section. Implicitly we have assumed that the effective

external cross sections A^* are the same for the fluxes of matter and momentum and for the kinetic pressures. Equation (3) can be simplified by the substitution of (1):

$$P_g = (Z\dot{N}_i + \dot{N}_g)\,\frac{k_B T^*}{w_z^* A^i} + \frac{\dot{N}_g m w_z^*}{A^i} + \Delta P_v\,. \quad (4)$$

Here Z is the effective charge number of the ions:

$$Z = n_e^*/n_i^*\,. \quad (5)$$

In this formulation the momentum balance, with the exception of Z and ΔP_v, can be checked by measurements of P_g, T^*, w_z^*, $\dot{N}_g$, and $\dot{N}_i$.

We estimate the viscous pressure decay as follows. The kinetic viscosity η^i of the mixture of neutral particles and ions inside the tube contains four contributions [26]: that of the ions, that of the neutrals and two mutual contributions. In our parameter range ($n_i \cong 10^{21}\,\mathrm{m}^{-3}$ and $n_a \cong 10^{22}\,\mathrm{m}^{-3}$, as we will see) the viscosity is largely a result from ion-ion collisions. The neutral particles may have some influence; their mean free path is limited mainly by collisions with the ions. So, the plasma viscosity may be somewhat larger than the ion viscosity $\eta^i = n_e k \hat{T}_i \tau_{ii}$ which is

$$\eta^i = \frac{2.1 \cdot 10^{-5}\,\hat{T}_i^{5/2}}{\ln \Lambda}\,, \quad (6)$$

and around $2 \cdot 10^{-5}$ for $\hat{T}_i \cong 2$ eV and $\ln \Lambda \cong 6$.

Here $\hat{T}_i$ is the ion temperature in eV and $\ln \Lambda$ is the Coulomb logarithm. So, we estimate the plasma viscosity η^i to be lower than 10^{-4} kg/ms.

To be sure that the viscosity is not turbulent, we will evaluate the Reynolds number of the flow inside the tube. As we will see the longitudinal drift velocity w_z^i has a value of about 10^3 m/s. Also a rotation w_θ^i occurs [4, 25] as a consequence of the Lorentz force by the radial current in the longitudinal magnetic field.

From previous measurements [12] it is known that in the external column w reaches values in excess of 100 m/s. A decrease below this value is observed if one approaches the cathode. Inside the cathode the ion neutral friction dominates in view of the large neutral density and smaller rotational velocities are to be expected. So, the axial component determines the velocity:

$$w^i \cong w_z^i\,. \quad (7)$$

Table 1. The data set inside the cathode as used for the energy balance equations.

w_{zi}^i	$1 \cdot 10^3$ m s^{-1}	$\dot{N}_i^{sat}$	$1.6 \cdot 10^{19}$ s^{-1}
n_a^i	$1 \cdot 10^{22}$ m^{-3}	$\dot{N}_g$	$3 \cdot 10^{20}$ s^{-1}
n_i^i	$1 \cdot 10^{21}$ m^{-3}	P_g	$3 \cdot 10^3$ Pa
$\hat{T}_i$	2 V	I_a	50 A

The resulting Reynolds number, calculated with the parameterset listed in Table 1

$$Re = w_z^i R_1 n_a^i m/\eta^i\,, \quad (8)$$

has a value of about 20. This value is too small for turbulence and therefore the viscosity is the kinetic one of (6).

Now we are able to estimate the viscous pressure decay ΔP_v along the tube. Because of the effective momentum coupling between the wall and the plasma, the viscous pressure decay should be due mainly to velocity shear:

$$\Delta P_v \cong \eta^i w_z^i L/R_1^2\,. \quad (9)$$

We calculate a value of about 10^2 Pa.

2.3. *Energy conservation*

The power dissipation can be formulated for two systems: the metal tube and the plasma inside it [8]. We will start with the combination of the two.

The supplied power is roughly the current I multiplied by the Debye sheath potential V_D, reduced by the tantalum threshold potential (electron emission work function) $V_w = 4.1$ V [27]. The thermal and convective power carried by the outcoming flow for each particle species j is $\dot{N}_j(\frac{5}{2} k_B T_j^* + \frac{1}{2} m_j w_{zj}^{*2})$ and in the incoming flow $\dot{N}_g(\frac{5}{2} k_B T^b + \frac{1}{2} m w_z^{b2})$. The outflux of potential energy roughly equals $N_i e V^*$ where $e V^* = 15.8$ eV, the ionization energy of argon I. We neglect multiple ionization here. Also the excited level densities are neglected with respect to the nearby ion ground level density [28].

A power dissipation mechanism of major importance is the thermal radiation by the outer cathode surface with outer radius R_2 and at a temperature T_c. The power is $\varepsilon \sigma_{SB} T_c^4 2\pi R_2 L$. Here σ_{SB} is the Stefan-Boltzmann constant and ε is the relative radiation emissivity of tantalum [27]. The length of the hot zone, L^h, has a minimum value because of the heat conduction in the metal through

which a power flux is transferred of $2KT_c/L^h$, where K is the thermal conductivity [27] at high temperature. The balance of these two effects reads

$$\varepsilon\sigma_{SB}T_c^4\pi R_2 L^h \cong 2KT_c\pi(R_2^2 - R_1^2)/L^h . \quad (10)$$

We note that the heat conduction is negligible provided that the cathode has a length of at least a few times L^h. This is the case in our experiments, as we will see. Now L^h can be calculated from (10):

$$L^h \cong (2K(R_2 - R_1)/\varepsilon\sigma_{SB}T_c^3)^{1/2} . \quad (11)$$

As a conclusion we write the energy balance of the cathode including the internal plasma column as

$$\begin{aligned} I_a(V_D - V_w) = \sum_j \dot{N}_j(\tfrac{5}{2}k_B T^* + \tfrac{1}{2}m_j w_z^{*2})_j \\ - \dot{N}_g(\tfrac{5}{2}k_B T^b + \tfrac{1}{2}m w_z^{b2}) \\ + \dot{N}_i e V^* + \varepsilon\sigma_{SB}T_c^4 2\pi R_2 L^h . \end{aligned} \quad (12)$$

Next we consider the tantalum tube itself. The arc current I_a at the inner cathode surface is sustained by free electron emission (I_e) and the bombardment of ions which all recombine (I_i). The tube is cooled by heat radiation and by the emission power $I_e V_w$ of free electrons. The heating is due to photon capture (P_f), ion collisions and neutral particle collisions. Arriving ions transfer to the cathode their recombination energy eV^* and a fraction β of their kinetic energy gained in the sheath minus the electron work function. We neglect the thermal energy of the ions and the (Bohm) energy with which they enter the sheath [14, 29]. The fraction β contains an uncertainty because the tantalum surface may be covered by one or more monolayers of carbon; we take $\beta = 0.5$ [30]. The neutral particle bombardement heats up the cathode with a frequency $\nu^i_{coll,a} \cong n_a^i \bar{v}_a^i \pi R_1 L/2$ where $\bar{v}_a^i = (8k_B T_a^i/\pi m)$. We are able now to write the energy balance of the tube:

$$\begin{aligned} I_e V_w + \varepsilon\sigma_{SB}T_c^4 2\pi R_2 L \cong I_i(\beta V_D + V^* - V_w) \\ + \nu^i_{coll,a}\beta\tfrac{3}{2}k_B(T^i - T_c) + P_f . \end{aligned} \quad (13)$$

We note that, in addition to statements by other authors [18, 7], the possibility of a temperature jump $T^i - T_c$ is left open.

We defer the discussion on the energy balance of the internal plasma, which can be obtained by the mere combination of (12) with (13), to a later stage.

3. Experiments

The theoretical considerations of Section 2 will be our guide in experimenting. The data needed are n_e^*, w_z^*, T^*, A_i^* and A_a^* besides some externally adjustable arc parameters. We will measure with a cylindrical tantalum cathode of 3 mm inner and 4 mm outer radii and with a length of about 10 cm. The arc length is about 1.3 m but in this work we use only data in the vicinity of the cathode (Fig. 1), in particular at $z^* = 10$ mm. In order to obtain reproducible measurements we machine the cathode

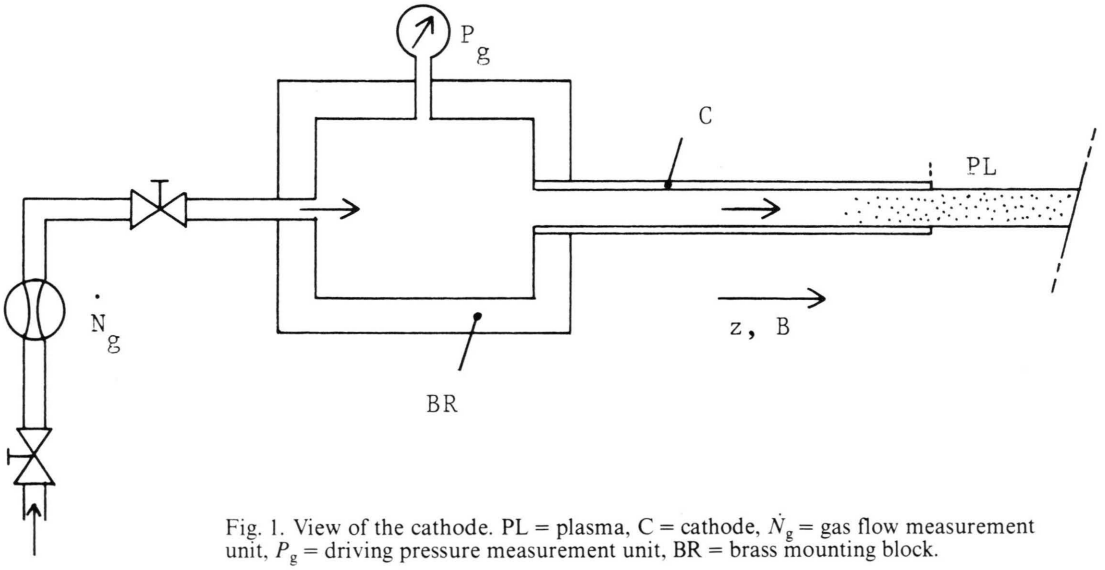

Fig. 1. View of the cathode. PL = plasma, C = cathode, $\dot{N}_g$ = gas flow measurement unit, P_g = driving pressure measurement unit, BR = brass mounting block.

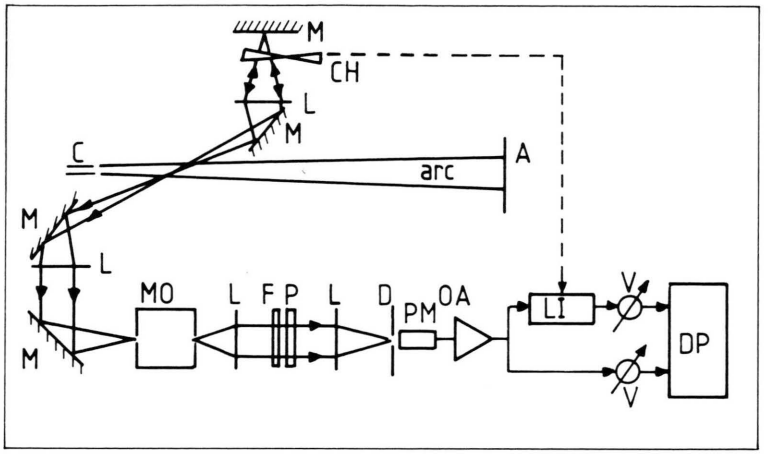

Fig. 2. Doppler shift diagnostic, C = cathode, A = anode, L = lens, M = mirror, CH = chopper, MO = monochromator, FP = Fabry-Pérot interferometer plates, D = pinhole diaphragm, PM = photomultiplier tube, OA = operational amplifier, LI = lock in amplifier, V = electrometer, DP = digital processing.

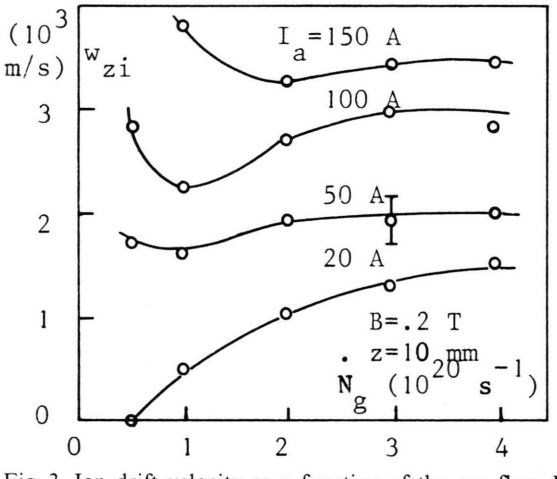

Fig. 3. Ion drift velocity as a function of the gas flow $\dot{N}_g$ for different arc currents.

such that it is always operated with a flat end. In this way we get the velocity measurements at intervals of several burning hours reproducibly within 5–15%. We measure only on the arc axis.

As far as the diagnostic equipment has been described elsewhere, we will refer to existing literature [4, 12, 13, 24, 25, 31].

3.1. Drift velocities of ions and neutrals

The external longitudinal drift velocities w_z^* of the ions and the neutrals have been measured by Fabry-Pérot interferometry of the Doppler shift of the 668.4 and 696.5 nm spectral lines respectively (Fig. 2) [24].

In Fig. 3 the w_z^* of the ions is given as a function of the gas flow. An increase of w_z^* with I_a and a saturation at high gas flows $\dot{N}_g$ can be noticed. At lower $\dot{N}_g$ the w_z^* increases again.

A supersonic drift velocity is measured at a weak B field (Figure 4). This corresponds with measurements by Theuws [22, 23]. The ion thermal velocity $v_{ti}^* = (2k_B T_i^*/m)^{1/2}$ decreases and w_{zi}^* increases strongly as B decreases.

Obviously in the first 10 mm between the cathode exit and the measurement point a considerable acceleration of the gas/ion mixture occurs because the plasma pressure of the external column (4) ceases to supply the balancing pressure against P_g. We not that the expansion in $0 \lesssim z \lesssim 10$ mm is by no means adiabatic because here the arc current still passes through a voltage difference $\Delta V \cong 3\,V$ with a power dissipation comparable with the plasma thermal output power of the cathode: $I_a \Delta V \cong \dot{N}_g e \hat{T}$. Here $\hat{T} = k_B T/e$ is the temperature in eV. The supersonic w_z^* indicates excellent possibilities for optimizing hollow cathode sources of particle beams [31]. At the weak B condition the w_z^* still turns out to depend on $\dot{N}_g$ (Fig. 5) and I_a (Figure 6). In the foregoing we have assumed implicitly that the w_z^* of ions and neutrals is equal up to $z = 10$ mm. This is confirmed in Fig. 7 where both are shown separately.

The neutrals exhibit an expansion so that w_z increases somewhat up to $z = 20$ mm. The consecutive decrease can be explained as follows. The neutral particle density is made up of a hot fraction coming out of the cathode and a cold fraction due to the

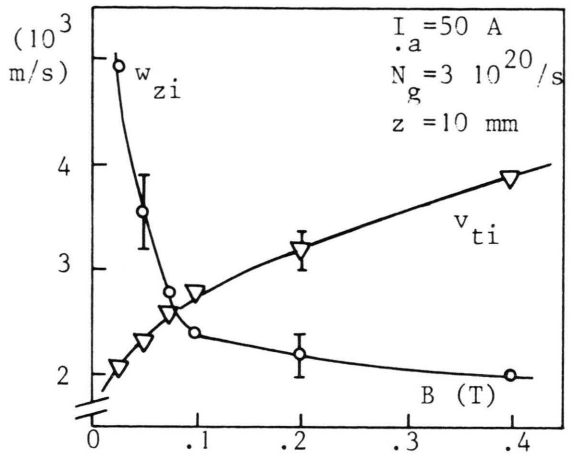

Fig. 4. Ion thermal (v_{ti}) and drift (w_{zi}) velocities as a function of the B field.

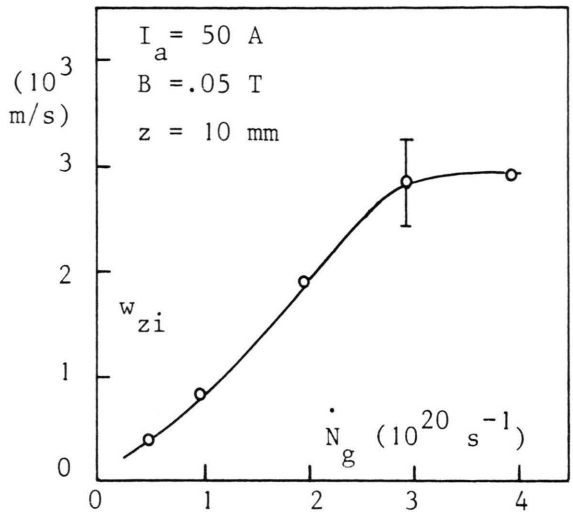

Fig. 5. Ion drift velocity as a function of the gas flow at weak B field.

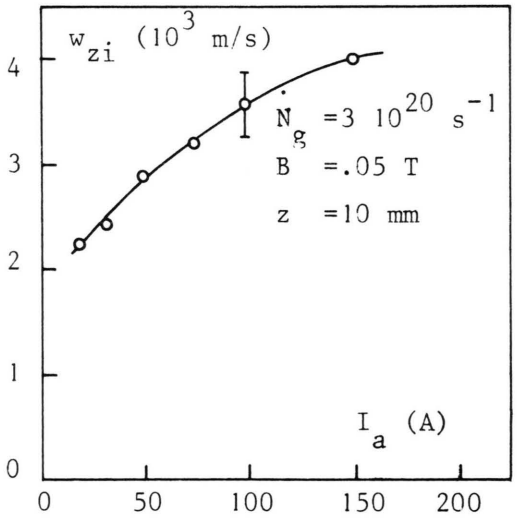

Fig. 6. Ion drift velocity as a function of the arc current at weak B field.

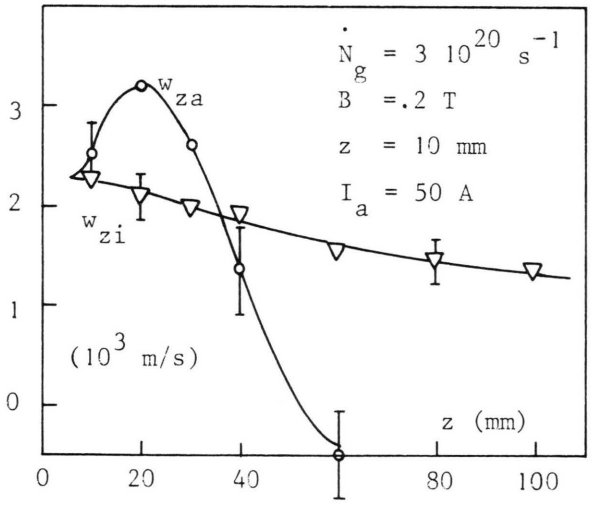

Fig. 7. Drift velocities of ions (w_{zi}) and neutrals (w_{za}) as a function of the longitudinal position.

surrounding gas background. The cold fraction hardly contributes to w_z so, as with increasing z the hot fraction decreases, w_z tends to 0.

The same physics is reflected in Figure 8. Here the Zeeman splitted Ar I 969.5 nm profile is displayed, as scanned with a Fabry-Pérot interferometer [24] for the measurement of w_z. Differently from temperature measurements, which are done under an observation angle of 90° with the axis, the velocity measurements are carried out under an angle of 25°.

In the latter case the Zeeman splitting cannot be filtered out. In the determination of w_z however this in no serious problem. Figure 8a shows the broad profile of hot neutrals near the cathode ($z = 10$ mm) while Fig. 8c shows the narrower profile of the cold particles at $z = 100$ nm. The mixture in Fig. 8b at $z = 340$ mm clearly exhibits the axial drift of the hot

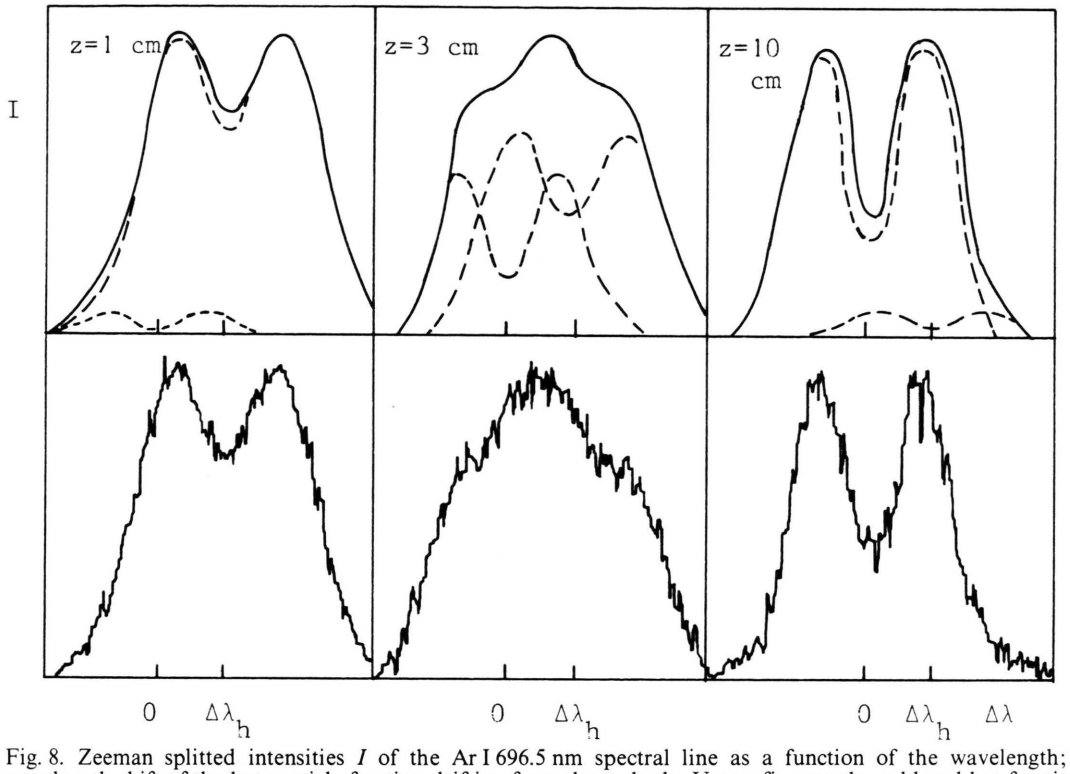

Fig. 8. Zeeman splitted intensities I of the Ar I 696.5 nm spectral line as a function of the wavelength; $\Delta\lambda_h$ is the wavelength shift of the hot particle fraction drifting from the cathode. Upper figures: the cold and hot fractions (dashed) and the resulting profile (drawn) at different distances z from the cathode. Lower figures: the actual measurements.

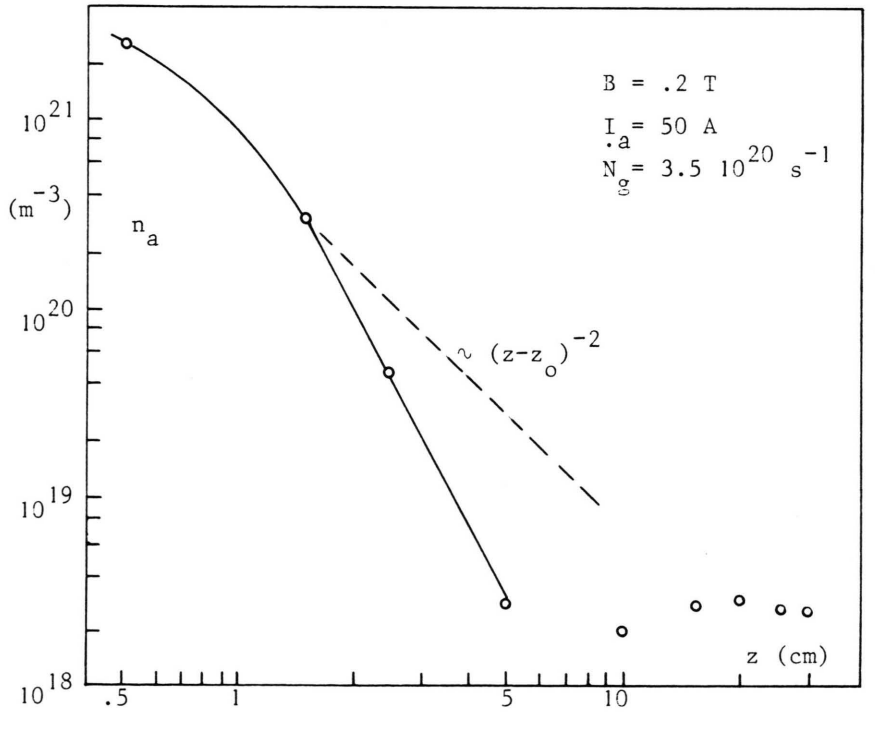

Fig. 9. Neutral particle density as a function of the longitudinal position. Dashed curve: the decrease in the case of free expansion.

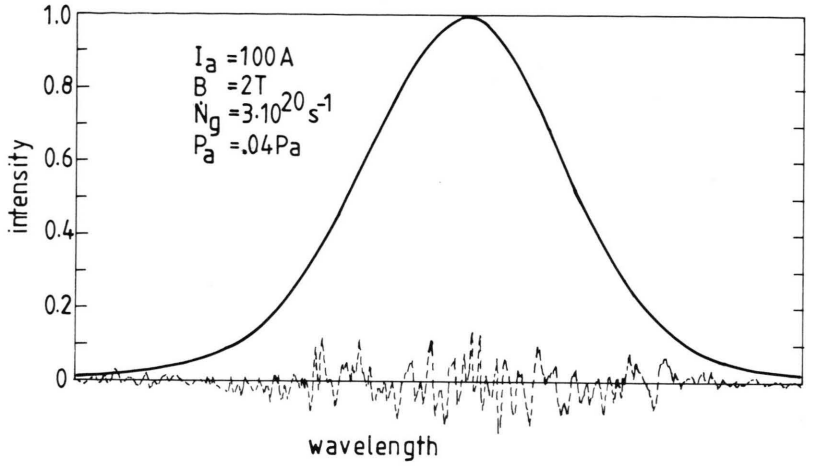

Fig. 10. Measured intensity of the 668.4 nm ion spectral line as a function of the wavelength. Dotted curve: the calculated Voight function; dashed: the residual × 10.

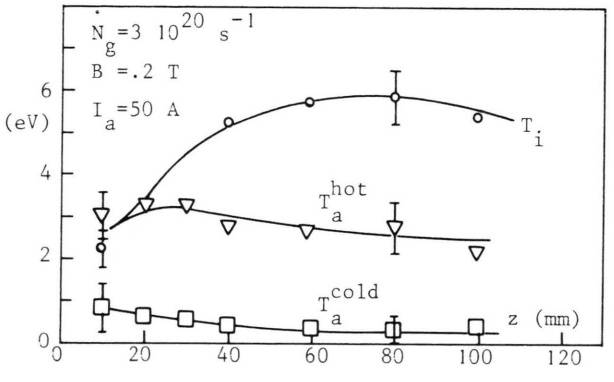

Fig. 11. Temperatures of the ions (T_i) and of the hot an cold neutrals (T_a) as a function of the longitudinal position.

neutrals because their profile is shifted with respect to that of the cold gas.

We also have observed another phenomenon (Figure 9). The neutral particle density decreases stronger with z than is to be expected from free expansion. Habets et al. [32, 33] give a virtual source model for the expansion of a monoatomic gas from a nozzle into vacuum. Situating the virtual source point on $z = 0.15\,R_1 = 0.45$ mm, we expect for $z > 2.5$ mm an expansion according to $n_a \cong (z - z_0)^{-2}$.

We have measured n_a by relating it to the density of the Ar I 4p group, using the density ratio method by Pots [13, 25, 24]. In Fig. 9 it appears that n_a decreases stronger with z than according to $(z - z_0)^{-2}$.

At $z = 20$ mm we estimate the mean free path z_f for the neutral gas in the z direction. The ionization frequency ν_{ion} [24] of the neutrals, both direct [34] and stepwise [35], is $4 \cdot 10^5\ s^{-1}$, so $z_f = w_z/\nu_{ion} \cong 8$ mm. The elastic and charge exchange collision frequency ν_{ai} is about $3 \cdot 10^5\ s^{-1}$ [24] so that the neutrals are confined somewhat by the ions. The quoted numbers for ν_{ion} and ν_{ai} refer to the following plasma-parameters: $n_e \cong 2 \cdot 10^{20}/m^3$, $\hat{T} \cong 5$ eV.

3.2. *Particle temperatures*

We have measured the ion temperature with the Doppler broadening of the 668.4 nm spectral line and the neutral gas temperature with that of the 696.5 nm line. We have obtained the temperatures after Voigt deconvolution of the Fabry-Pérot intensity profile (Figure 10).

The plasma has been observed under an angle of 90° with the axis, so that the π-Zeeman component can be selected [24] and the influence of the splitting is minimized.

Our assumption that the temperatures of the different particle species are equal up to $z = 10$ mm because of the high density, finds confirmation for the ions and the neutrals in Figure 11. We have separated the Ar I line profile into two Voigt functions of which one represents the hot gas coming with the ions out of the cathode and the other the colder neutral background contribution. This picture corresponds with our interpretation of Figs. 7 and 8.

In Figs. 12–15 we give the ion temperatures in dependence of $\dot{N}_g$, I_a and B. We notice a decrease of T_i^* with $\dot{N}_g$, but an increase with I_a and B.

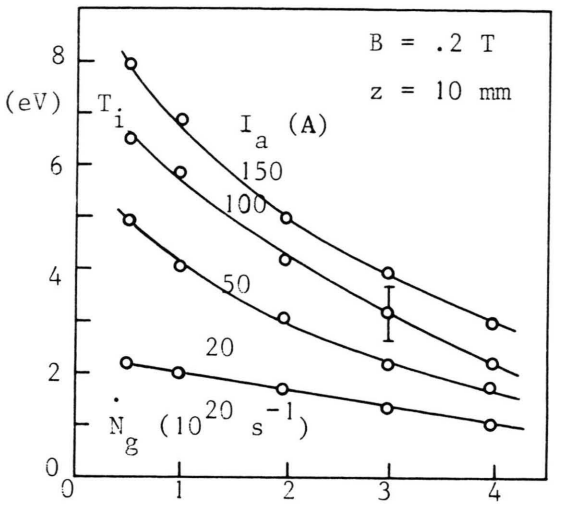

Fig. 12. Ion temperatures as a function of the gas flow at different arc currents.

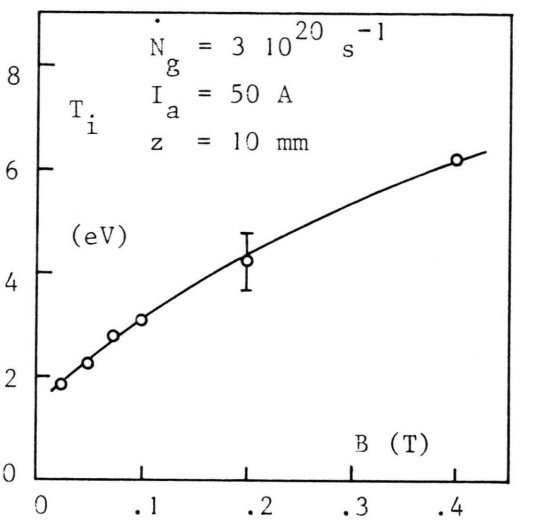

Fig. 13. The ion temperature as a function of the magnetic field strength.

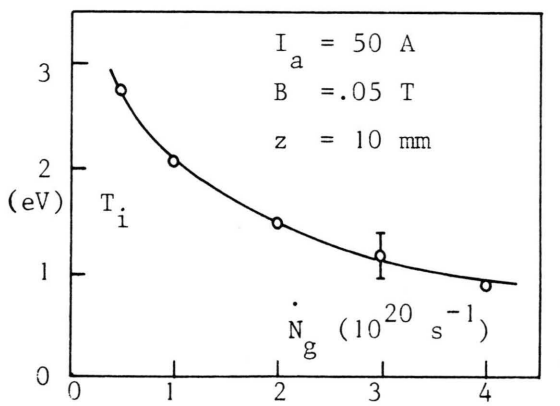

Fig. 14. The ion temperature as a function of the gas flow at weak B field.

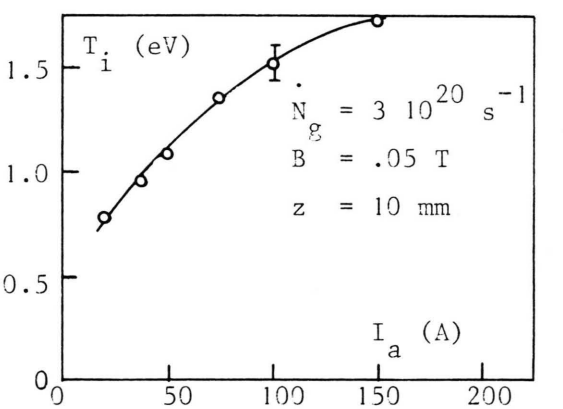

Fig. 15. The ion temperature as a function of the arc current at weak B field.

In Fig. 12 we see ion temperatures that must exceed the electron temperatures. In that case the ions are heated neither by the electrons, nor by the neutrals. Viscous heating must play a dominant role then [4, 13].

3.3. *Electron densities*

The electron density is established from the plasma continuum radiation [24]. A Thomson scattering measurement [36] serves as a calibration.

We have measured n_e with varying $\dot{N}_g$, B and I_a as is shown in the Figures 16–19. We see that only variations of I_a influence n_e strongly.

From Fig. 20 it appears how n_e decreases with z. An extrapolation towards $z = 0$ indicates a value for n_e of 10^{21} m^{-3} at the cathode tip.

We note that Fig. 20 indicates a radial expansion of the plasma from $z = 1$ cm towards $z = 2.5$ cm. The expansion factor would be 2.3 in area, if the plasma was source free and no ionization occurred. However, as mentioned, ionization is present which

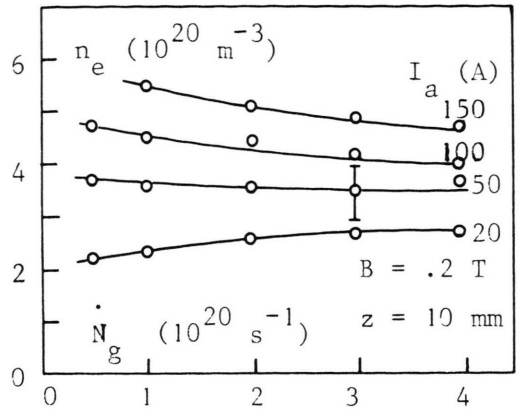

Fig. 16. The electron density as a function of the gas flow at different arc currents.

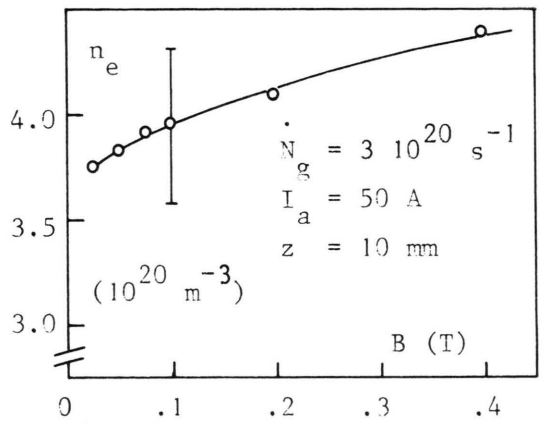

Fig. 17. The electron density as a function of the magnetic field strength.

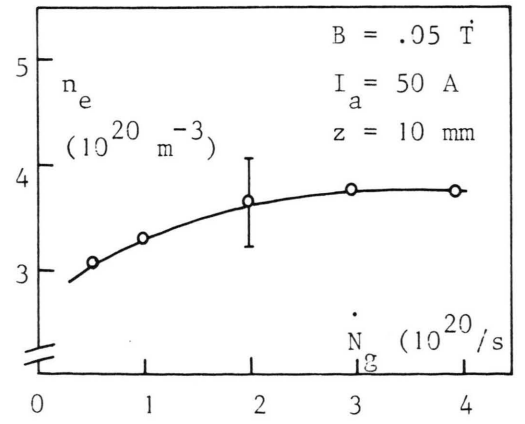

Fig. 18. The electron density as a function of the gas flow at weak *B* field.

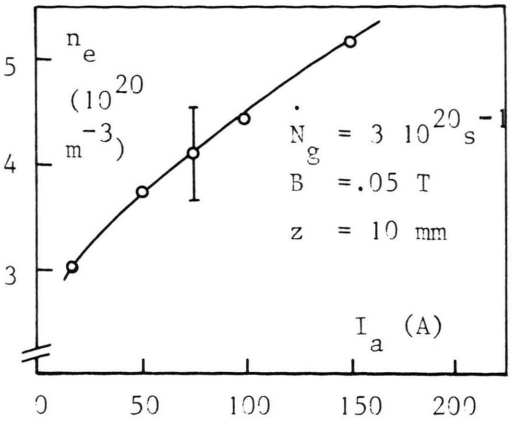

Fig. 19. The electron density as a function of the arc current at weak *B* field.

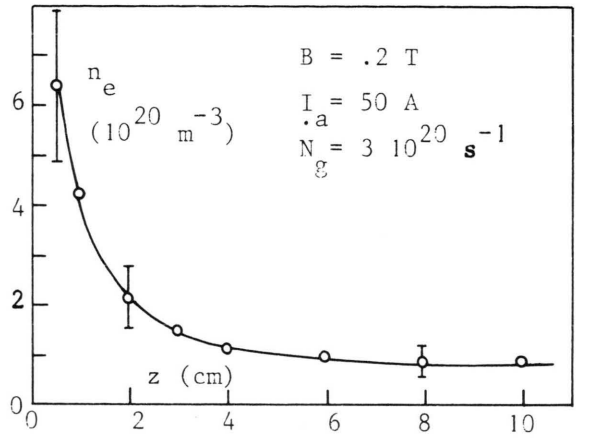

Fig. 20. The electron density as a function of the longitudinal position.

leads to a stronger decrease of n_a with z than according to free expansion (Figure 9). Taking this source terms for electrons and ions into account, we find an expansion factor of approximately 3.5. Using previous measurements [24] where an effective plasma radius $R_{\text{eff}} = 5.5$ mm has been found at $z = 2.5$ cm, this expansion factor corresponds with an $R_{\text{eff}} \cong 3.0$ mm at $z = 1.0$ cm. Apparently, the effective plasma radius is about equal to the cathode radius R_1, which is confirmed by other observations.

3.4. Driving pressure and arc voltage

The momentum balance (4) contains the driving pressure P_g of the neutral gas entering the cathode

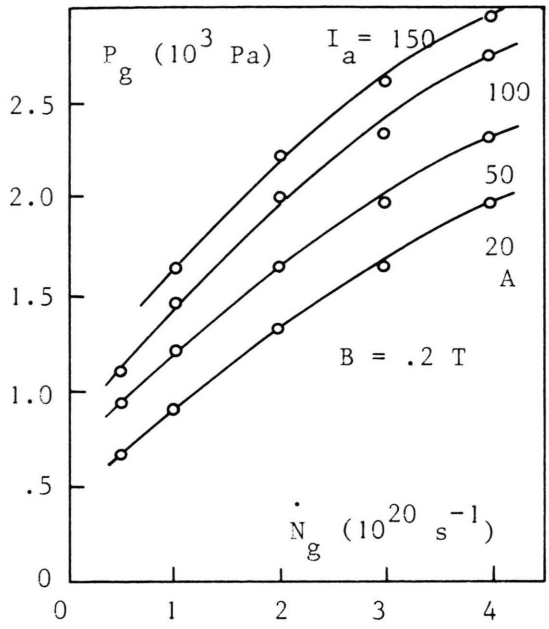

Fig. 21. The neutral gas driving pressure as a function of the gas flow at different arc currents.

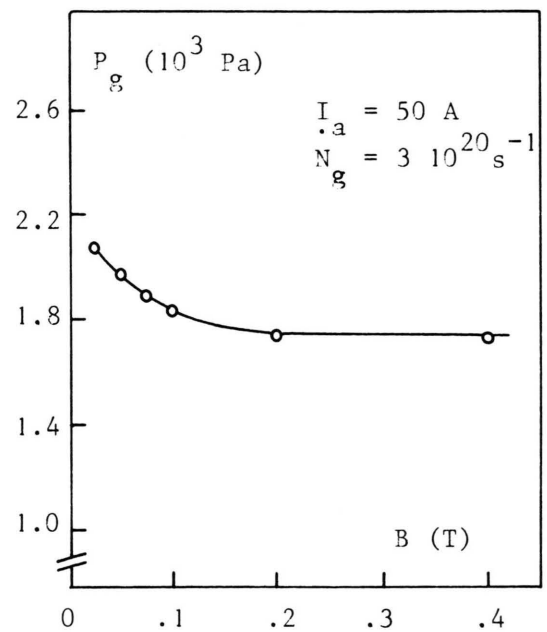

Fig. 22. The neutral gas driving pressure as a function of the magnetic field strength.

(Figure 1). The measurements of P_g are given in the Figs. 21 and 22. The increase of P_g with $\dot{N}_g$ and I_a is considerable.

The arc voltage V_{ak} is interesting so far as the properties of the external arc remain the same and only variations in the cathode, mainly the sheath, are observed (Figs. 23 and 24). We note that at $I_a = 20$ A the voltage is irregular with respect to the other measurements. The low current arc [8] is

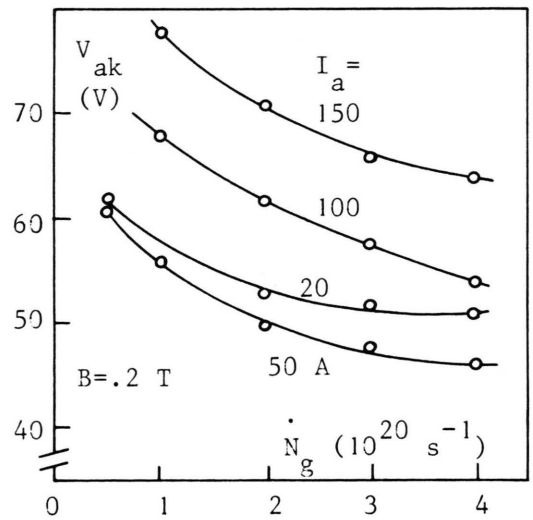

Fig. 23. The arc voltage as a function of the gas flow at different currents.

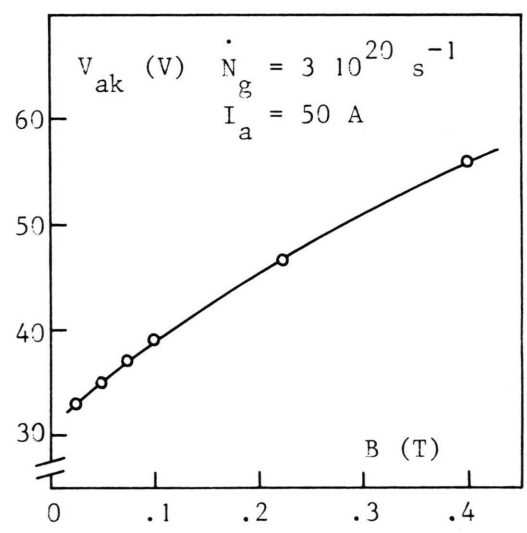

Fig. 24. The arc voltage as a function of the magnetic field strength.

known to form hot spots, which may be the cause of the irregularity.

4. Discussion

We will discuss the consequences of our experimental results regarding the theoretical considerations of section 2.

4.1. Matter conservation

As a first subject we consider the conservation of mass (1). Our measurements have been carried out at the axis of the plasma, although also information on the cross section A_i^* at $z = 10$ mm is needed. In the discussion on Fig. 20 we have noticed a radial plasma expansion so that a value of about πR_1^2 for A_i^* should be expected. With the supposition that the effective charge number Z (5) is unity, this leads to an ion flow rate $\dot{N}_i$ approaching the incident gas flow rate $\dot{N}_g$ in the small flow case. This means that the fraction of neutrals being ionized reaches 100% as shown in Figs. 25 and 26.

The measured ion beam intensity is consistent with previous measurements [24]. These indicate ion flow rates $\dot{N}_i$ of $4 \cdot 10^{19}\,s^{-1}$ at $z = 2.5$ cm, $I = 50\,A$, $B = 0.2\,T$ and $\dot{N}_g = 3.5 \cdot 10^{20}\,s^{-1}$.

In Fig. 26 it is seen that $\dot{N}_i$ saturates towards high gas flows. As has been our expectation in Sect. 2 the ion saturation production $\dot{N}_i^{sat}$ is connected with

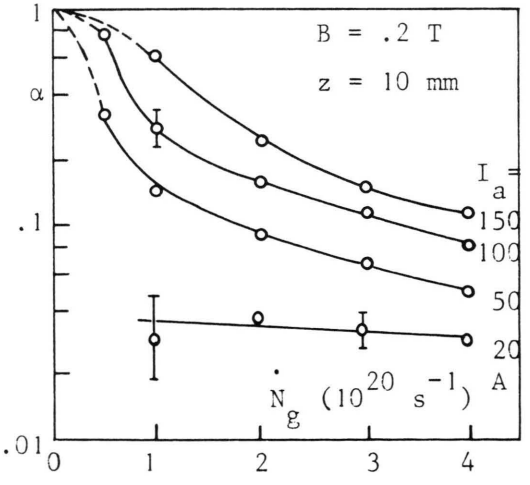

Fig. 25. The ionization fraction ($\alpha = \dot{N}_i/\dot{N}_g$) as a function of the gas flow at different currents.

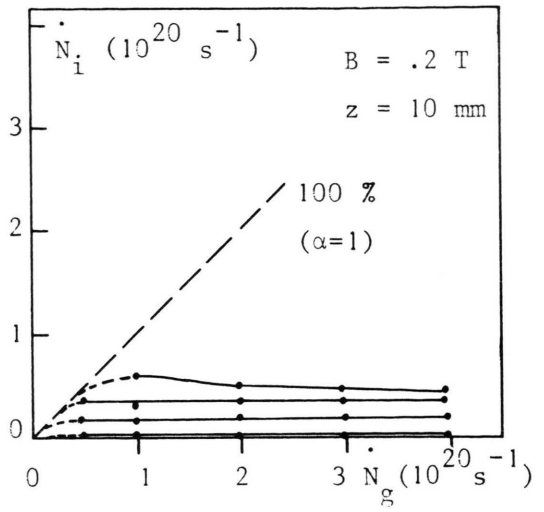

Fig. 26. The ion production rate as a function of the gas flow at the different currents of Figure 25.

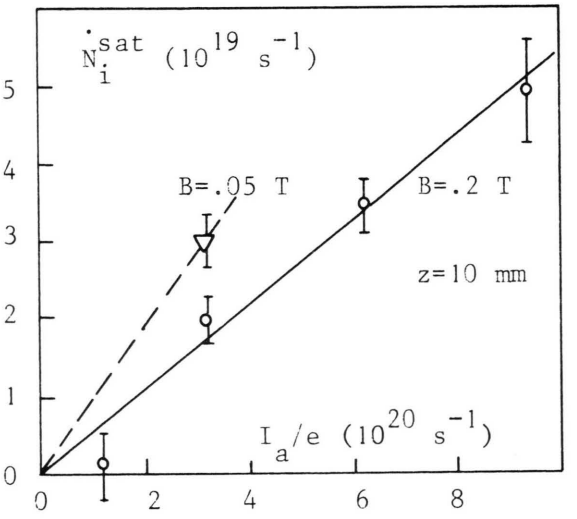

Fig. 27. The saturation value of the ion production rate at high gas flow rate, as a function of the arc net charge carrier flux (I_a/e).

I_a/e. We conclude from Fig. 27 that the dependence is linear:

$$\dot{N}_i^{sat} = c\, I_a/e\,, \tag{14}$$

where the constant $c = 0.05$ at $B = 0.2\,T$. The value of c is somewhat smaller than given in [31]. For a weak magnetic field a somewhat higher value for c applies.

A literature survey by Delcroix and Trindade [8] shows that a number of experimenters with hollow

cathode arcs has chosen a $\dot{N}_g$ in the vicinity of $0.05\, I_a/e$, with this rate as a mean value. Assuming that these experimenters have varied $\dot{N}_g$ around $\dot{N}_i^{sat}$, we suggest that (14) may have a general validity for hollow cathodes.

We will now estimate the ratio ξ of the ion production within the cathode and the volume ionization in the external arc. Volume recombination may be neglected [37]. With an arc length L_a and radius R_a we write

$$\xi = \frac{\dot{N}_i}{\pi R_a^2 L_a n_e n_a \langle \sigma v_e \rangle_{ion}} . \tag{15}$$

Taking $\dot{N}_i = 0.05\, I_a/e$ at $I_a = 50\, A$, $R_a = 10^{-2}$ m [38], $L = 1$ m, $n_e = 8 \cdot 10^{19}\ m^{-3}$, $n_a = 5 \cdot 10^{18}\ m^{-3}$, $\langle \sigma v_e \rangle_{ion} = 4.7 \cdot 10^{-15}\ m^3/s$, $\hat{T}_e = 5$ V and a factor 1.74 for stepwise ionization [34, 35], we obtain $\xi \cong 0.03$. The volume ionization in the external arc is much larger than the production by the cathode. The strong dependence however of $\langle \sigma v_e \rangle_{ion}$ on T_e does not allow conclusions about ξ for the hollow cathode arc in general.

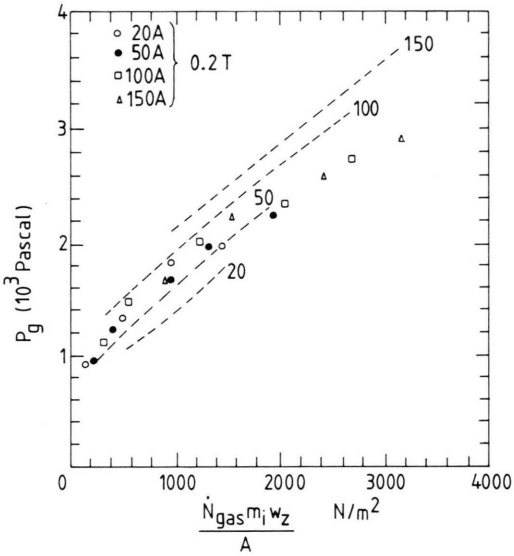

Fig. 28. Solid curve and open symbols, the measured driving gas as a function of the momentum flux $\dot{N}_g m w_z^x / A^i$ at different currents. Dashed curve, the with aq. 4 computed driving gas pressure as a function of the momentum flux $\dot{N}_g m w_z^x / A^i$ at different currents. Dashed curve: the actually measured pressure.

4.2. *Momentum conservation*

As is seen in our measurements of w_z^* and $\hat{T}_i^*$, no linear proportionality between v_{ti}^* and w_z^* is present. At $z = 10$ mm the ion flow cannot a priori be considered as sonic.

We find however that the driving pressure P_g is a function of $\dot{N}_g m w_z^*/A^i$, the convective momentum flux at $z = 10$ mm (4). In Fig. 28 it appears that, regardless the value of I_a, for a given B field the w_z^* is determined by the choice of P_g and $\dot{N}_g$. The measured P_g is compared with that calculated from (4) with insertion of measured data (dashed curve in Figure 28). Here, the viscous decay ΔP_v has been omitted since the calculated value of about 10^2 Pa falls well within the uncertainty margin.

It is observed that there is a good agreement between the measured and calculated values for P_g.

4.3. *Energy conservation*

In order to get insight in the main energy conversion processes in the cathode, we will estimate the magnitudes of the terms in the (11), (12), and (13).

First we check whether the length L^h of the hot cathode zone (11), corresponds with the visual estimate of about 1.5 cm. At a temperature T_c of 3000 K tantalum has a K of 60 W/mK and an ε of 0.3 [27]. With $R_1 = 3$ and $R_2 = 4$ mm and a σ_{SB} of $5.67 \cdot 10^{-8}\ W/m^2K^4$ we calculate $L^h = 1.6$ cm. We note that according to (11) the tube temperature in the hot zone cannot decrease much below 3000 K. The melting point of tantalum is 3269 K [27], so also much higher temperatures are excluded.

Next we consider the ion density n_i^i inside the cathode. The ions recombine on the hot inner cathode wall with a rate $\dot{N}_i^{coll} = n_i^i \bar{v}_i\, 2\pi R_1 L/4$.

We follow Resenov et al. [16, 17] by assuming that a considerable fraction of I_a is sustained by ion wall recombination. This leads to $I_a \cong e\dot{N}_i^{coll}$.

Taking $\hat{T}_i = 2$ eV, $I_a = 50\, A$ and $L = 2$ cm we obtain $n_i^i = 9 \cdot 10^{20}\ m^{-3}$. This value corresponds with the ion production rate $\dot{N}_i$ if the internal ion drift velocity

$$w_z^i \cong 10^3\ m/s ,$$

for

$$\dot{N}_i \cong n_i w_z^i \pi R_1^2 \cong 2 \cdot 10^{19}\ s^{-1} \cong \dot{N}_i^{sat} .$$

The assumed $\hat{T}_i$ is roughly consistent with the longitudinal momentum balance inside the cathode.

Taking a $\dot{N}_g \cong n_a^i w_z^i \pi R_1^2 \cong 3 \cdot 10^{20}\,s^{-1}$ we obtain $n_a^i \cong 10^{22}\,m^{-3}$. A pressure of $3 \cdot 10^3$ Pa (Fig. 28) then leads to $\hat{T}_i \cong 2$ eV. For still another reason a n_a^i of about $10^{22}\,m^{-3}$ and consequently a $\hat{T}_i$ of 2 eV is to be expected. The Paschen curve [39] for electrical breakdown in argon has its minimum near 1 Pa m at room temperature. With as a characteristic length $L/2 \cong 1$ cm this leads to a density $n_a^i \cong 2 \cdot 10^{22}\,m^{-3}$. A n_a^i near $10^{22}\,m^{-3}$ is at the given cathode dimension an optimum density for electrical breakdown. Consequently in cathodes of a smaller dimension a higher n_a^i is to be expected, as is indeed observed [23].

With these data (Table 1) we calculate the terms in (12). With the omision of some apparently negligible contributions we write

$$\underset{1.3\,kW}{I_a (V_D - V_w)} = \underset{0.3\,kW}{\dot{N}_g (2.5\, e\, \hat{T}^* + 0.5\, m_i w_z^{*2})} + \underset{0.3\,kW}{2.5\, I_a \hat{T}^*} + \underset{0.04\,kW}{\dot{N}_i e V^*} + \underset{0.7\,kW}{\varepsilon \sigma_{SB} T_c^4 2\pi R_2 L}\,. \quad (16)$$

We see that the energy balance of the cathode and the internal column together is dominated by heat radiation as the main power loss mechanism and by the current over the voltage drop as the main power input. The thermal and convective power losses with the neutrals, ions and electrons however is not negligible.

In order to check the balance of the tantalum tube itself, we first have to estimate the photon heating P_f in (13). The P_f consists of plasma continuum radiation and line radiation. The continuum radiation [40, 41] inside the volume $\pi R_1^2 L$ contributes about 0.05 kW. The line radiation volume power dissipation arises mainly from Ar I 4p–4s transitions. From extensive collisional radiative studies according to v.d. Sijde et al. [42] we estimate the 4p density to be at most a factor of 10^3 above the Saha population [28] which can be calculated on the basis of n_e^i and $\hat{T}_a^i$. A density $n_a(4p) < 1.3 \cdot 10^{18}\,m^{-3}$ and a resulting contribution to P_f smaller than 0.006 kW is calculated. As a conclusion we estimate P_f to be about 0.05 kW.

Now we estimate the terms in (13). As an example we use $I_e = 20$ A and $I_i = 30$ A:

$$\underset{0.08\,kW}{I_e V_w} + \underset{0.7\,kW}{2\pi R_2 L \varepsilon \sigma_{SB} T_c^4} = \underset{0.05\,kW}{P_f} + \underset{0.8\,kW}{I_i (\beta V_D - V_w + V^*)} + \underset{0.35\,kW}{\dot{N}_a^{coll} \beta 1.5\, e (\hat{T}^i - \hat{T}_c)}\,. \quad (17)$$

From this balance we see that the radiative cooling power is mainly supplied by collisions of ions and neutral particles. From (17) it is clear that indeed I_i sustains a considerable fraction of I_a, for the neglect of I_i would lead to an unacceptably small energy supply.

The energy balance of the ionized gas inside the cathode can be estimated from a combination of (16) and (17). We only consider the terms of at least 0.1 kW:

$$\underset{1.3\,kW}{I_a (V_D - V_w)} = \underset{0.3\,kW}{\dot{N}_g (2.5\, e\, \hat{T}^* + 0.5\, m_i w_z^{*2})} + \underset{0.3\,kW}{2.5\, I_a \hat{T}^*} + \underset{0.8\,kW}{I_i (\beta V_D + V^*)} + \underset{0.35\,kW}{\dot{N}_a^{coll} \beta 1.5\, e (\hat{T}^i - \hat{T}_c)}\,. \quad (18)$$

The main heating mechanism is still the current passing the sheath voltage. The internal column is for the most part cooled by ions that escape towards the wall their ionization energy $e V^*$.

We have seen in Fig. 23 that V_D decreases as $\dot{N}_g$ increases. In (18) the V_D plays an important role: the decrease of V_D diminishes the plasma power input although more particles leave the cathode and $\dot{N}_a^{coll}$ increases. We conclude that at increasing $\dot{N}_g$ the ion wall recombination I_i should contribute more to I_a because the I_e decreases with the decreasing field enhanced emission of electrons from the surface.

5. Conclusions

We have carried out experiments on the source properties of a hollow cathode. For a number of arc conditions accurate measurements of the ion drift velocity, the temperature and the electron density have been performed. With these data, combined with the arc parameters, we may draw some conclusions.

The ion drift velocity at weak B fields is significantly larger than the ion thermal speed. This supersonic flow is of interest for hollow cathode particle sources. A low B field is also appropriate for source applications because the external arc is not turbulent in that case [38].

The neutral particle density in the first few centimeters of the external arc is determined by the expansion from the cathode. A fraction of the expanding neutrals is as yet ionized there. At larger

distances the neutral background density of the vessel dominates.

The ion production rate $\dot{N}_i$ of the cathode increases with increasing gas flux $\dot{N}_g$ and saturates at 5% of I_a/e, the net arc charge carrier flux. So a high ion production rate, close to 100%, with a low gas waste can be obtained by drawing a strong arc current with limited gas flux. Also the ionization in the external arc is effective; only in the first few cm the ion influx from the cathode plays a significant role.

The neutral gas driving pressure P_g just before the cathode entrance is a function of the produced convective momentum flux, regardless the arc current. This implies that the ion output drift velocity w_z^* is a function of $\dot{N}_g$ and P_g. It can therefore be adjusted by a choice of the latter parameters.

The energy balance of the cathode with its internal column shows that the strongest power input arises from the arc current that crosses the Debye sheath. This is dissipated mainly in the form of heat radiation from the cathode surface and for a minor part by the kinetic energy of the outgoing particles. The tube itself is mainly heated by ion collisions.

It appears that a considerable part of the arc current at the inner cathode surface is sustained by recombining ions. The plasma inside the cathode gains its power from the arc current over the sheath and loses most of it by ion recombining collisions at the wall.

Acknowledgement

The authors thank Dr. Lunk and Mr. de Haas for their contributions to the optical diagnostics in earlier work. The assistence with the measurements and the technical support by Mr. van der Sande are gratefully acknowlegded. We thank Mrs. Groenendijk and Mrs. Gruyters for the preparation of the manuscript.

[1] J. S. Luce, Proc. 2nd Unit. Nations Conf. Peaceful Uses Atom. Energy **31,** 305 (1958).
[2] L. M. Lidsky, S. D. Rothleder, D. J. Rose, S. Yoshikawa, C. Michelson, and R. J. Mackin, J. Appl. Phys. **33,** 2490 (1962).
[3] J. L. Delcroix, Physique des Plasmas, Dunod, Paris 1966.
[4] B. F. M. Pots, Thesis Eindhoven Univ. Technol. (1979).
[5] J. L. Delcroix, H. Minoo, and A. R. Trindade, Rev. Roum. Phys. **13,** 401 (1968).
[6] J. L. Delcroix, H. Minoo, and A. R. Trindade, Journ. de Phys. **29,** 605 (1968).
[7] A. Lorente-Arcas, Plasma Phys. **14,** 651 (1972).
[8] J. L. Delcroix and A. R. Trindade, Hollow Cathode Arcs in Advances in Electronics and Electron Physics, Vol. **35,** Academic Press, New York 1974.
[9] V. I. Miljevic, Phys. Lett. **92 A,** 439 (1982).
[10] J. Uramoto, J. Vac. Soc. Jap. **20,** 170 (1977).
[11] G. Ecker, K.-U. Riemann, and Ch. Wieckert, Beitr. Plasmaphys. **22,** 463 (1982).
[12] D. C. Schram, J. J. A. M. van der Mullen, B. F. M. Pots, and C. J. Timmermans, Z. Naturforsch. **38a,** 289–303 (1983).
[13] B. F. M. Pots, P. van Hooff, D. C. Schram, and B. van der Sijde, Plasma Physics **23,** 67 (1981).
[14] D. Bohm, in Characteristics of Electrical Discharges in Magnetic Fields, McGraw-Hill, New York 1949.
[15] D. E. Siegfried and P. J. Wilbur, Int. Electr. Propuls. Conf., Las Vegas 1981.
[16] S. P. Resenov and A. Lunk, Beitr. Plasmaphys. **18,** 101 (1978).
[17] S. P. Resenov and A. Lunk, Beitr. Plasmaphys. **18,** 381 (1978).
[18] C. M. Ferreira and J. L. Delcroix, J. Appl. Phys. **49,** 2380 (1978).
[19] A. I. Hershovitch and V. J. Kovarik, Rev. Sci. Instrum. **54,** 328 (1983).
[20] S. Tanaka, H. Morita, and J. Sakuraba, Jap. J. Appl. Phys. **19,** 1703 (1980).
[21] P. G. A. Theuws, H. C. W. Beijerinck, D. C. Schram, and N. F. Verster, J. Appl. Phys. **48,** 2261 (1977).
[22] P. G. A. Theuws, H. C. W. Beijerinck, N. F. Verster, and D. C. Schram, J. Phys. E. Sci. Instrum. **15,** 573 (1982).
[23] P. G. A. Theuws, Thesis Eindhoven Univ. Technol. (1981).
[24] J. M. M. J. Vogels, J. C. M. de Haas, D. C. Schram, and A. Lunk, J. Appl. Phys. **59,** 71 (1986).
[25] C. J. Timmermans, A. Lunk, and D. C. Schram, Beitr. Plasma Phys. **21,** 117 (1981).
[26] S. Chapman and T. G. Cowling, The Mathematical Theory of Non-Uniform Gases, Cambridge University Press, London 1970, SBN 521-07577-7.
[27] R. C. Weast and S. M. Selby ed., C.R.C. Handbook of Chemistry and Physics 48th ed., Ohio 1967.
[28] M. Mitchner and C. H. Kruger, Partially Ionized Gases, Wiley, New York 1973, ISBN 0-471-61172-7.
[29] J. M. M. J. Vogels, Internal rep. Eindhoven Univ. Technol. (1977), in Dutch.
[30] H. H. Brongersma, private communication.
[31] J. M. M. J. Vogels, L. U. E. Konings, V. Koelman, and D. C. Schram, XVI Intern. Conf. Phenom. Ioniz. Gases, Düsseldorf 1983, p. 486.
[32] A. H. M. Habets, Thesis Eindhoven Univ. Technol. (1977).
[33] H. C. W. Beijerinck and N. F. Verster, Physica **111C,** 327 (1981).
[34] H. W. Drawin, Zeitschr. Phys. **164,** 513 (1961).

[35] J. J. A. M. v. d. Mullen, B. v. d. Sijde, B. F. M. Pots, and D. C. Schram, XIII Intern. Conf. Phenom. Ioniz. Gases, Berlin 1977.
[36] B. v. d. Sijde, S. Adema, J. de Haas, C. J. M. Denissen, and M. J. F. v. d. Sande, Beitr. Plasmaphys. **22,** 357 (1982).
[37] K. Katsonis, Thesis Univ. Paris-Sud (1976).
[38] J. M. M. J. Vogels, Thesis Eindhoven Univ. Technol. (1984).
[39] G. F. Weston, Cold Cathode Glow Discharge Tubes, ILIFFEE Books Ltd., London 1968.
[40] L. Spitzer, Physics of Fully Ionized Gases, Wiley, New York 1962.
[41] R. J. Rosado, Thesis Eindhoven Univ. Technol. (1981).
[42] B. v. d. Sijde, J. J. A. M. v. d. Mullen, and D. C. Schram, Beitr. Plasmaphys. **24,** 447 (1984).